Microstructure and hydro-mechanical behaviour of compacted granular bentonite

Hao Zeng[1*], *Laura* Gonzalez-Blanco[2,1], *Enrique* Romero[1,2], and *Alessandro* Fraccica[3]

[1]Universitat Politècnica de Catalunya (UPC), Barcelona, Spain
[2]International Centre for Numerical Methods in Engineering (CIMNE), Barcelona, Spain
[3]Italian Institute for Environmental Protection and Research (ISPRA), Rome, Italy

Abstract. In recent years, granular bentonite GB has become a reference material since it facilitates the backfilling operation due to high-density compacted granules with extended grain size distribution (maximum sizes around 10 mm). This investigation explores the initial microstructure of MX80-type GB and the hydro-mechanical HM response observed at the phenomenological scale. Samples were statically compacted at a fixed dry density (1.55 Mg/m^3), encompassing dry and wet sides of the optimum. The microstructural study was performed using a combination of X-ray micro-computed tomography and mercury intrusion porosimetry. The results indicate that the pore size density function of compacted GB can be simplified as a double-porosity network with micropores (intra-granular/aggregate pores) and macropores (inter-granular/aggregate pores). Compacting at the dry side increases macropores, making the sample more compressible on loading under as-compacted states despite the higher matric suction. The time evolution of the swelling pressure displays a double-peak pattern attributed to the particular microstructure of the samples. Moreover, the initial microstructure does not significantly influence the water retention properties without a marked hysteresis in the high-suction range under confined wetting/drying cycles. This work's outcomes highlight the microstructure's significance in the HM behaviour of compacted GB and provide further insight into the geotechnical properties of this material.

1 Introduction

Bentonite-based composites own desirable merits of low permeability, high swelling potential and effective self-sealing [1-2]. Thus, they have been selected to produce buffer/backfill materials in deep geological storage facilities for high-level and long-lived radioactive nuclear wastes [3]. Bentonites are also vital components of Geosynthetic Clay Liner (GCL) systems used for separating municipal and industrial contaminants from the bio-phase [4]. In the service period of these systems, bentonites likely encounter complicated hydro-mechanical HM stress paths [3]. For example, from the assemblage of buffer/backfill materials to the running of repositories, bentonites will suffer from compaction, desiccation under tunnel environments, hydration with water from near host rocks, and subsequently swelling in free/confined conditions [5-6]. Furthermore, bentonite constituents in GCLs, initially displaying high total suction, must be hydrated to achieve a certain degree of saturation before emplacing the wastes [4]. Hence, an in-depth understanding of the HM behaviour of bentonites is necessary to estimate the long-term safety of bentonite barriers.

Granular bentonite GB manufactured by crushing heavily-compacted bentonite units (pellets) at low water content and dry densities close to 2.0 Mg/m^3 has been proposed to be a reference buffer/backfill material in recent years [5-7]. The granular bentonite includes powder and high-density granules with an extended grain size distribution (maximum grain sizes around 10 mm). Therefore, this material has a more optimal particle size distribution than other bentonite types (e.g. powder and pellet bentonites) [5-6]. Moreover, the granular bentonite with better pourability and workability facilitates backfilling and compaction operation in horizontal drifts or geotextiles, while avoiding the creation of more dust [8]. However, the use of GB is still quite limited due to the reduced studies on the evaluation of its HM performance.

This work aims to narrow the knowledge gap on the HM behaviour of compacted GB and its microstructure. MX-80 type GB samples were compacted at different water contents and at a dry density of 1.55 Mg/m^3 to evaluate their HM behaviour, including compressibility on loading, swelling pressure and water retention capacity. The microstructural inspection of compacted bentonite samples leads to a better interpretation of the results at the phenomenological scale. The outcomes from this investigation emphasise the importance of the initial microstructure on the HM behaviour of compacted GB.

* Corresponding author: hao.zeng@upc.edu

2 Material

2.1 Tested bentonite

The tested samples were made up of MX-80 sodium type GB (Fig. 1a). The montmorillonite content of this bentonite approximates 90%, and the total specific surface is 523 m^2/g [5-6]. The solid density (ρ_s) at 20°C was determined to be 2.75 Mg/m^3 (ASTM D854-14) using a pycnometer with non-polar ethyl alcohol. The plastic and liquid limits, determined according to ASTM D4318-17, were 77% and 515%, respectively. The particle size distribution was carried out by dry sieving method and without crushing (Fig. 1b), ranging the well-graded GB from fine grains to high-density granules with large sizes (10 mm) with a curvature coefficient C_c =1.59 and uniformity coefficient C_u =21.6. As observed, no significant fraction of GB was detected at grain sizes < 75 μm.

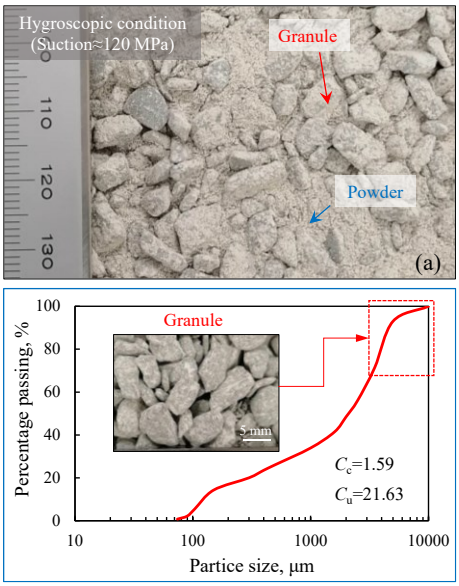

Fig. 1. (a) MX-80 type GB; (b) Particle size distribution by dry sieving and without crushing.

2.2 Compaction protocol

Under laboratory conditions (T = 20°C and RH = 50%), the GB at a hygroscopic water content of 6.5% was mixed with de-aired water to different water contents: 16.0%, 20.0% and 26.0%. An airtight bag sealed the wetted material for at least 48 hours to ensure uniform water distribution within the entire mass. Afterwards, the wetted bentonite was subjected to static compaction at a vertical displacement rate of 0.5 mm/min to achieve a dry density of 1.55 Mg/m^3. Before unloading at the same rate, the maximum compaction stress was retained for 1 hour. In the end, the size of each sample was 20 mm in height and 50 mm in diameter. The initial state of the compacted samples, including the initial total suction and the compaction stress, were summarised in Table 1.

Table 1. Initial state of compacted GB samples.

Sample ID	S1	S2	S3
Water content, w_0, %	16	20	26
Dry density, ρ_d, Mg/m^3	1.55	1.55	1.55
Degree of saturation, S_{r0}	0.55	0.72	0.93
Total suction, MPa	40	22	9
Compaction stress, MPa	5.0	5.5	6.0

3 Testing protocols

3.1 Compressibility tests

Compacted samples at different initial water contents were placed in an oedometer cell to undergo stepwise loading up to a maximum vertical stress of 10 MPa (σ). During testing, the vertical displacement was recorded by an LVDT with a resolution of 1 μm, to assess the change in the void ratio (e). The compression curves were used to analyse the yield stress and the pre- and post-yield compressibility indexes κ and λ (defined as $-\Delta e/\Delta ln\sigma$), respectively.

3.2 Swelling pressure

The compacted samples at different initial water contents were gradually wetted under isochoric conditions. The wetting was conducted with a water pressure of 200 kPa at the sample's bottom cap, using a standard pressure/volume controller with a resolution of 1 kPa. The outflow was under atmospheric conditions. The sample was considered fully saturated when the outflow rate was equivalent to the inflow rate. During the wetting process, a miniature load cell (maximum load 20 kN, accuracy less than 0.2%), monitored the development of the total vertical stress.

3.3 Water retention behaviour

To assess the water retention behaviour, the compacted samples were prepared inside a metallic cell with an internal size of 30 mm in diameter and 6 mm in height [5]. The samples first experienced wetting by placing them in a vapour saturated environment (RH=100%). The porous cover of the cell allowed the sample to exchange water vapour with the external environment, while the metallic wall limited the volumetric swelling to maintain a constant volume condition. At different intervals of the wetting stage, the sample was sealed with a membrane for 3 days to ensure uniform water distribution. Then, the cell was inserted into a dew point

psychrometer (WP4, Decagon Devices with 0.1-300 MPa measurement range) for total suction measurement. Afterwards, the water content was determined by checking the mass change of the sample. When this step finished, the sample continued to be wetted in the vapour saturated environment. The whole wetting was completed when the water content increased to about 28% (i.e. to a degree of saturation close to 1). Subsequently, drying under laboratory conditions (RH=50%) acted on the samples. The same method was used to measure the total suction and water content. As a result, the water retention curve of the compacted samples under constant volume could be obtained in a wetting/drying cycle.

4 Results and discussion

4.1 Microstructural analysis

Micro-CT was employed as a non-destructive 3D technique to observe the microstructure of cylindrical subsamples (10 mm in height and 7 mm in diameter) taken from the tested samples. The CT scanner 'SkyScan 1272 desk-top X-ray microtomography' has a measurement resolution (voxel) of 4×4×4 μm^3. The obtained microstructure was reported in a greyscale image stack (16 bits). Denser material results in the greater incident X-ray energy being attenuated [9]. In the CT image of bentonite materials (Fig. 2), the voxels with darker colours represented low-density phases such as air or water, while those with brighter colours indicated high-density solid particles [10]. The CT slices of the compacted bentonite samples with different water contents revealed the microstructure under as-compacted states, with local heterogeneity in bulk density distribution. The heterogeneity tended to reduce with increasing compaction water content, e.g. 26%.

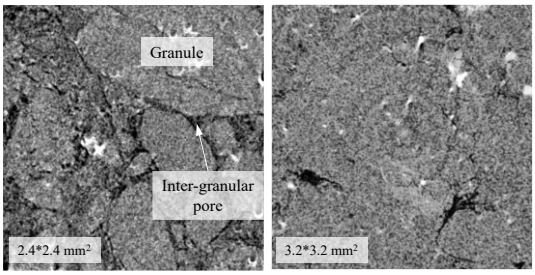

(a) w_0=16%_as-compacted (b) w_0=26%_as-compacted

Fig. 2. CT slices of bentonite samples under different as-compacted states.

Furthermore, a region of interest (3D ROI) inside the CT image stack can be transformed into a histogram in terms of voxel count versus grey value using the software ImageJ (Fig. 3a). Since the void ratio of the sample was known (void ratio associated with the CT measurement range), a grey threshold (T) can be defined to segment the pore phase from the entire stack. In the image segmentation, the white voxels were pores and the black ones were solids (Fig. 3b). The ImageJ plugin 'Pore Size Distribution' [11] was run on the binary ROI to simulate the mercury intrusion process. As a consequence, the cumulated intrusion volume normalised by the volume of solids (non-wetting void ratio, e_{nw}) and the entrance pore size (x) were associated with the ROI. Thus, the CT images could be used to quantitively analyse the pore pattern of the tested materials.

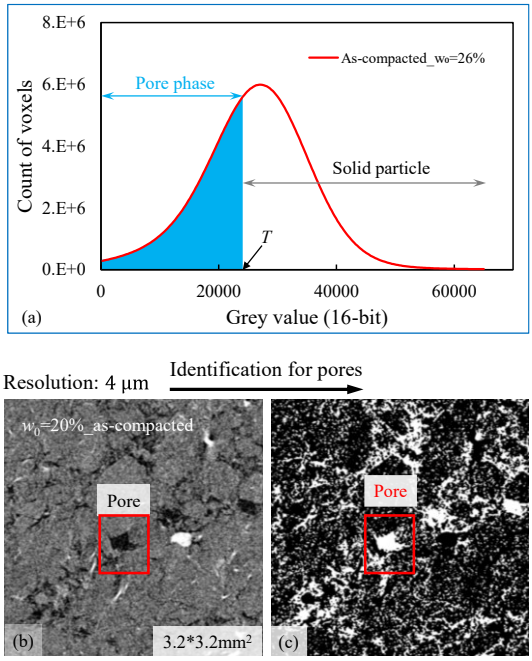

Fig. 3. Image segmentation for pore identification.

Mercury intrusion porosimetry MIP tests were also performed to assess the pore network of small cubes (10×10×10 mm) trimmed from the tested samples. The cubes were first freeze-dried since it was required for this technique. A porosimeter 'AutoPore IV 9500 - Micrometrics Instrument Corp' was used with the smallest detected pore size of approximately 8 nm. The MIP technique determined the absolute pressure driven by a non-wetting liquid (mercury) to enter the empty pores and the invasive mercury volume. According to the Washburn equation and assuming that the pores are cylindrical in shape or parallel to infinite plates, x and e_{nw} can be calculated [12]. To better identify the entrance pore size mode, the pore size density function (PSD) was considered as $PSD = -(de_{nw}) / log\ (dx)$.

However, MIP technique has some limitations [12]. For instance, at low injection pressure, it is not easy to discern the compression behaviour of the GB from large-pore intrusion, inducing the injected mercury volume to fluctuate and making it difficult to identify the large-pore modes. Moreover, freeze-drying can induce the formation of fissures, especially in materials at high water content and with significant clay content. These limitations might be salient in examining the pore size distribution of GB using MIP, since the material's microstructure is heterogeneous and includes many large-size pores (Fig. 2). The cumulative curves by MIP of the non-wetting void ratio indicated that the sample compacted at a higher water content (26%) displayed more large-size pores (Fig. 4a). Therefore, MIP data are not entirely consistent with Micro-CT results, in which

larger pore sizes were detected at drier states (Fig. 2). Gonzalez-Blanco & Romero (2019) [10] observed a large number of fissures between large-size granules in compacted GB after freeze-drying, using Micro-CT (Fig. 4c). Hence, Micro-CT, which did not require freeze-drying, was used to obtain the cumulative non-wetting void ratio curves within its measurement range of large sizes. Compared to MIP results, the CT data, within its resolution, did not show pores with sizes larger than 100000 nm in the as-compacted sample (Fig. 4d). However, freeze-dried samples at a similar hydraulic state displayed entrance pore sizes larger than 100000 nm, in both CT image method and MIP. The phenomenon confirms some influences of freeze-drying on the pore analysis, particularly at large pore sizes. In addition, Micro-CT analyses may include pores enclosed around solid particles and pores isolated by smaller ones. Thus, at a given final entrance pore size of 8000 nm, the image method provided a slightly higher non-wetting void ratio (Fig. 4d).

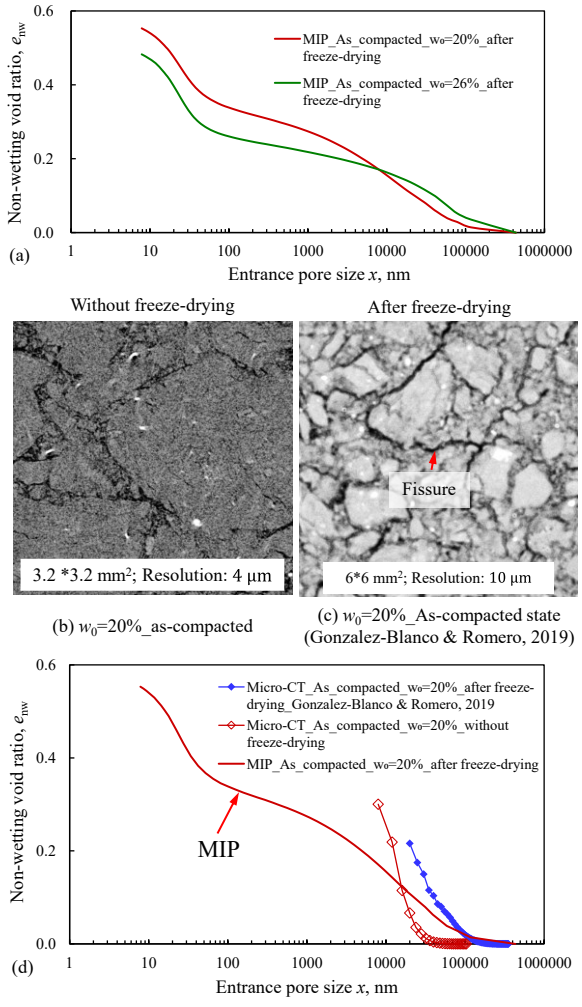

Fig. 4. (a) Cumulative intrusion curves of compacted GB from MIP; (b)-(c) CT slices of compacted GB before and after freeze-drying; (d) Comparison of cumulative non-wetting curves of GB before and after freeze-drying using image analysis method and MIP.

As discussed above, the pore size and volume estimation at the macro-scale can be better evaluated through the imaging technique on samples without freeze-drying. In light of this, the microstructural analyses in the current work were established on the results from MIP for entrance pore sizes < 8000 nm and integrated with Micro-CT for pore sizes > 8000 nm. The cumulative non-wetting void ratio curves and PSD functions determined by the combination of the two methods on samples under different as-compacted states indicated that lowering the compaction water content at a given dry density yields more detected large-size pores and a higher final e_{nw} (Fig. 5a). The PSD functions revealed that the compacted samples tended to a triple-porosity network, notably under low compaction water, e.g. 16% (Fig. 5b). The triple-porosity network likely involves intra-aggregate/granular and inter-aggregate pores inside granules and inter-granular pores between granules. For the sake of simplicity, the triple-porosity mode was considered as a double-porosity one: micropores inside aggregates/granules and macropores covering inter-aggregate/granular pores. The PSD functions suggest that a threshold entrance pore size of 300 nm can be defined to distinguish the micropores from the macropores. The threshold size is in agreement with that reported in previous investigations on MX-80 type bentonites [5, 13]. Within the micropore level, the dominant entrance pore size was about 20 nm, regardless of compaction water content [5]. The dominant size at the macropore scale changed with different as-compacted states at a fixed dry density. An increase in the compaction water content led to a smaller dominant size, as the granules disaggregated with absorbing water during sample preparation.

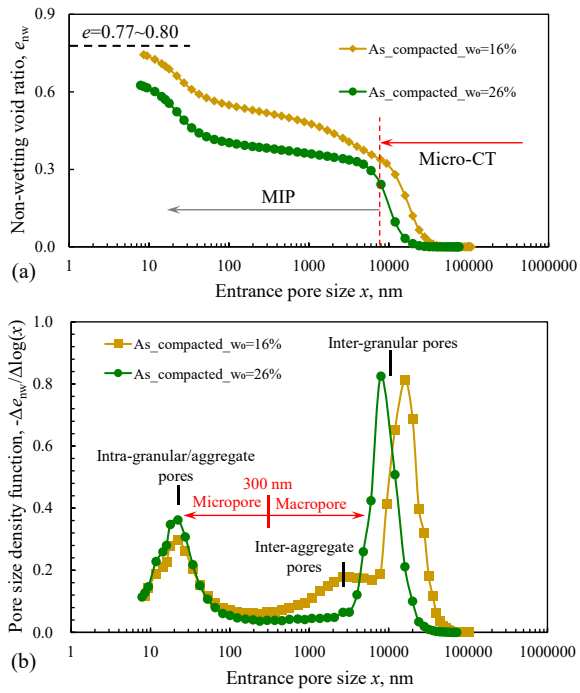

Fig. 5. (a) Cumulative curves of compacted GB samples resulted from Micro-CT and MIP; (b) PSD functions.

4.2 Mechanical response

The compression curves of the bentonite samples starting from diverse as-compacted states described that

at a given initial dry density, the compacted samples had similar pre-yield compressibility κ (Fig. 6). Increasing the compaction water content requires larger yield stress to arrange the granular structure associated with the lower macropore volume detected at high water contents (Fig. 5a) and despite the lower matric suction. Beyond yield stress, the post-yield compressibility of the drier sample is larger, linked to the higher macropore volume prone to collapse under loading.

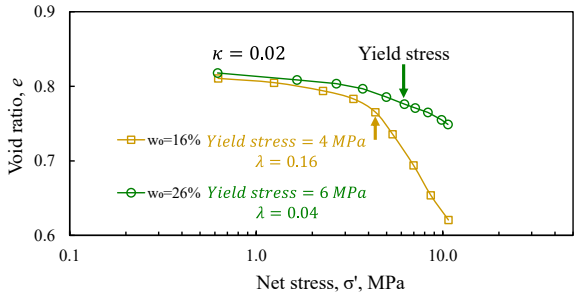

Fig. 6. Compression curves of compacted GB samples at a fixed dry density with different initial water contents.

4.3 Evolution of swelling pressure

The swelling pressure of the compacted samples at different initial water contents was measured along a wetting path under isochoric conditions (Fig. 7). The early stage of wetting induced the swelling pressure to increase followed by a plateau period, typically between 50 and 100 hours. Afterwards, the swelling pressure developed again, up to eventual stabilisation. The double pattern of swelling pressure may arise from the double-porosity network. During wetting, the macropores are initially flooded, reducing the matric suction prevailing in this domain and inducing the initial development of swelling pressure. On the other hand, the suction difference induces the drier granules to slowly absorb water from the macropores. Under certain conditions, some macropore suction increase may occur, as explained by [15]. Therefore, the global development of swelling pressure could be delayed, which causes the plateau observed.

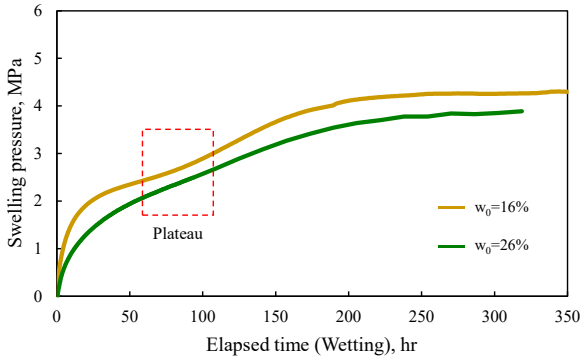

Fig. 7. Time evolution of swelling pressure of samples compacted at two initial water contents.

4.4 Water retention capacity within confined wetting/drying cycle

The nearly overlapped water retention curves on wetting of compacted samples with different initial water contents were determined at a condition of constant volume (Fig. 8). This fact means that the water retention behaviour in response to wetting is less affected by the initial microstructure. Seiphoori et al. (2014) [5] reported a similar water retention behaviour, using the same wetting path on the same GB compacted at various initial void ratios. Moreover, the microstructure of the compacted GB also evolves during wetting [5]. However, despite this microstructural evolution, no significant hysteresis in the subsequent drying path was observed. These results could be associated with the wetting/drying paths following the scanning curves. Along scanning curves, the water retention response is highly recoverable and quite insensitive to the initial microstructure and hydraulic history [5].

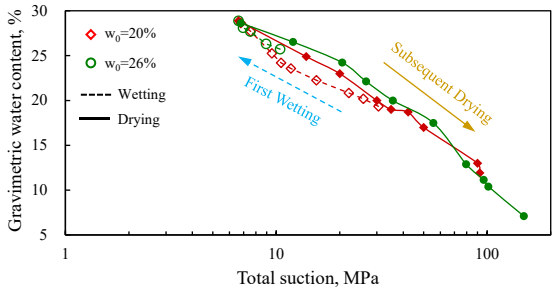

Fig. 8. Water retention curves along confined wetting/drying cycle on as-compacted GB samples at various initial water contents.

5 Concluding remarks

This work launched a series of HM tests on compacted GB. The phenomenological results were analysed based on microstructural studies, giving the following conclusions:

1. The microstructure of compacted granular bentonite has local heterogeneity. The components of the pore network are inter-granular, inter-aggregate and intra-aggregate pores, determined by the combination of Micro-CT and MIP described in the contribution. Nevertheless, when analysing the hydro-mechanical behaviour, the pore size distribution can be simplified by adopting a double-porosity model: macropores (inter-granular/aggregate pores) and micropores (intra-granular/aggregate pores). This double-structure information is helpful for simulations of the HM behaviour of GB that consider a discrete set of porous and homogeneous bentonite units, such as those recently presented by [16].
2. The higher proportion of macropores in samples compacted at low water content results in higher compressibility and lower yield stress despite the higher matric suction. The double-porosity model induces two periods of swelling pressure development. The initial growth of swelling pressure is related to the flooding of

macropores, while the absorption and expansion of micropores control the secondary development. Moreover, the water retention behaviour of compacted GB along wetting under constant volume is insensitive to the initial microstructure. The microstructural evolution by isochoric wetting also does not affect the water retention response on subsequent drying.

Acknowledgments
The authors acknowledge the support of the 'European Joint Programme on Radioactive Waste Management (EURAD)' (2019-2024) WP-Gas 'Mechanistic understanding of gas transport in clay materials' funded under H2020-Euratom with the grant agreement no. 847593. The first author has received funding from the China Scholarship Council (CSC).

References

1. Nagra. *The Nagra research, development and demonstration (RD&D) plan for the disposal of radioactive waste in Switzerland,* Nagra Technical Report NTB 09-06. Wettingen, Switzerland: Nagra. (2009)
2. C. Hoffmann, E.E, Alonso, E. Romero, Phys. Chem. Earth., **32(8-14)**, 832-849. (2007)
3. A. Gens, Géotechnique, **60(1)**, 3-74 (2010)
4. R.A. Beddoe, W.A. Take, R.K. Rowe, J. Geotech. Geoenviron., **137(11)**, 1028-1038 (2011)
5. A. Seiphoori, A. Ferrari, L. Laloui, Géotechnique, **64(9)**, 721-734 (2014)
6. A. Ferrari, J.A. Bosch, P. Baryla, M. Rosone, Acta Geotech., 1-12 (2022) (in press)
7. H. Ito, Appl. Clay Sci., **31(1-2)**, 47-55 (2006)
8. A. Seiphoori, L. Lalou, A. Ferrari, M. Hassan, W.H. Khushefati, Soils Found., **56(3)**, 449-459 (2016).
9. B. Zhao, J.C. Santamarina, Géotechnique, **70(2)**, 181-186 (2020).
10. L. Gonzalez-Blanco, E. Romero, *Hydro-mechanical processes associated with gas transport in MX-80 Bentonite in the context of Nagra's RD&D programme (results by May 2019).* Nagra Technical Report NAB 19-16, pp. 67 (2019)
11. B. Münch, L. Holzer, J. Am. Ceram. Soc., **91(12)**, 4059-4067 (2019)
12. E. Romero, P.H. Simms, Geotech. Eng., **26(6)**, 705-727 (2008)
13. E. Romero, G. Della Vecchia, C. Jommi, Géotechnique, **61(4)**, 313-328 (2011).
14. E.E. Alonso, A. Gens, A. Josa, Géotechnique, **40(3)**, 405-430 (1990).
15. E.E. Alonso, E. Romero, C. Hoffmann, Géotechnique, **61(4)**, 329-344 (2011).
16. V. Navarro, J. Torres-Serra, E. Romero, L. Asensio, Geomech. Energy Environ., **in press**, (2022).